

# Nonlinear analysis of NATM tunnel construction with the boundary element method

Plínio G.C. Prazeres<sup>a</sup>, Klaus Thoeni<sup>b,\*</sup>, Gernot Beer<sup>a</sup>

<sup>a</sup> Institute for Structural Analysis, Graz University of Technology, 8010 Graz, Austria

<sup>b</sup> Centre for Geotechnical and Materials Modelling, The University of Newcastle, NSW 2308, Australia

## ARTICLE INFO

### Article history:

Received 4 August 2010

Received in revised form 7 July 2011

Accepted 10 October 2011

Available online 24 November 2011

### Keywords:

Tunnelling

Three-dimensional NATM modelling

Boundary Element Method (BEM)

Finite Element Method (FEM)

Coupling BEM/FEM

Nonlinear analysis

Hierarchical constitutive model

Tunnel lining

## ABSTRACT

This paper presents a novel approach to the simulation of NATM tunnel construction using the Boundary Element Method (BEM) as principal numerical method. This new approach has the advantage that only the excavation surface, the possible plastic zones and the tunnel lining have to be discretised. The whole rock mass is represented by the BEM whereas the Finite Element Method (FEM) is used to represent the tunnel lining only. Thus, a general coupling strategy for coupling three-dimensional boundary elements with shell finite elements (shotcrete) and beam finite elements (steel arches) is presented. To achieve realistic results the effect of hydration of the shotcrete and yielding of the steel arches is considered in the excavation process. Furthermore, the nonlinear rock behaviour is modelled more realistically by using a powerful hierarchical constitutive model which considers a large range of rock materials. The combination of these ideas results in higher user-friendliness and efficiency. Some verification tests and practical applications in tunnelling are presented.

© 2011 Elsevier Ltd. All rights reserved.

## 1. Introduction

The New Austrian Tunnelling Method (NATM) is known to be an efficient method for the construction of tunnels which require a high flexibility to adapt to difficult and variable ground conditions. When driving tunnels according to the NATM, a complex process of sequential excavation and installation of ground supports takes place. The excavation sequence and the order of the installation of the ground support (shotcrete, steel arches and rockbolts) play an important role and nonlinear material behaviour has to be considered. A three-dimensional (3D) analysis has to be carried out in order to get realistic results. Since analytical solutions are available for a limited number of problems with very simple geometries only, the use of numerical tools is imperative.

For practical matters the tunnelling problem can be considered an infinite or semi-infinite domain problem. Thus, the Boundary Element Method (BEM) seems to be the most suitable numerical method because the far field is automatically considered due to the use of fundamental solutions. No mesh truncation errors are introduced and no artificial boundary conditions are required. Moreover, better accuracy is obtained in the stress evaluation with the BEM in comparison to other domain methods such as the Finite Element Method (FEM) and the Finite Difference Method (FDM) for

similar levels of discretisation as for example shown by Gao and Davies [13]. Nevertheless, the FEM is still the most popular numerical method for geotechnical problems.

A good overview of the developments and applications of numerical methods to tunnelling is given by Gioda and Swoboda [15]. The authors point out that most practical tunnelling problems are solved by using the FEM. Nevertheless, also the BEM was applied to tunnelling problems [27] but most of the work is in two-dimensions (2D) only. Only recently the BEM has been applied to 3D nonlinear problems [10,20,11,28]. However, the application of the method to real 3D NATM tunnelling problems has not been considered yet.

Researchers have worked on different approaches for the coupling of both methods. The usual approach consists in using the FEM to simulate the tunnel lining and the zones around the tunnel which undergo plastic deformation and in using the BEM to simulate the elastic zones of the rock mass. However, most of this work focuses on 2D modelling only [22,26,29]. Furthermore, the use of the BEM for the nonlinear zone and the direct coupling of the boundary elements with the finite elements for the tunnel lining has – to the best of the authors' knowledge – never been discussed in 3D. Pöttler and Swoboda [17] for example discussed how to couple beam elements and boundary elements in 2D only.

By using the standard formulation of the BEM to solve nonlinear problems, only the parts of the domain where yielding is expected and the boundary of the problem have to be discretised [23]. However, the size of the system of equation which has to be solved does

\* Corresponding author.

E-mail addresses: [plinioglauber@usp.br](mailto:plinioglauber@usp.br) (P.G.C. Prazeres), [klaus.thoeni@newcastle.edu.au](mailto:klaus.thoeni@newcastle.edu.au) (K. Thoeni), [gernot.beer@tugraz.at](mailto:gernot.beer@tugraz.at) (G. Beer).

not increase because of the domain discretisation. Thus, the dimension of the problem is still reduced by one.

Apart from the advantages of the BEM, a more accurate simulation of the tunnel lining, such as the shotcrete and the steel arch supports, is achieved by using shell and beam finite elements. Therefore, a general coupling strategy in combination with a multiregion approach as presented by Beer et al. [7], which is capable of giving the BEM the ability to simulate sequential excavation, is implemented in this work.

Moreover, regarding the modelling of the shotcrete, the effect of hydration (or curing) of the concrete may have a strong influence on the final results [19], and hence, it must be considered in the simulation. Concerning the steel arches, the effect of yielding elements also needs to be taken into account for some special cases, such as squeezing ground [18].

On top of that, an adequate model for the rock behaviour has to be considered to be able to realistically simulate the nonlinear rock mass. This can be achieved by the use of a hierarchical constitutive model able to consider the full range of different rock mass behaviour.

In this paper a new approach to directly couple beam and shell finite elements with boundary elements in 3D is presented. The whole rock mass is modelled by the BEM and a hierarchical constitutive model is used. In order to achieve realistic results the effect of hydration of the shotcrete and yielding of the steel arches is also considered in the excavation process. The combination of these new developments allows an adequate, efficient, accurate and elegant simulation of tunneling problems.

In the theoretical explanations – for the sake of simplicity – most of the figures refer to a 2D deep tunnel example. Nevertheless, the equations presented are directly applicable to general 3D problems and remarks concerning 3D analyses will be made whenever needed.

Verification tests and practical applications are presented, followed by some conclusions on the results obtained with the new approach.

## 2. Simulation of the rock mass with the BEM

A nonlinear analysis with the BEM requires special consideration in some parts  $\Omega_0$  of the domain  $\Omega$  where plastic behaviour is expected [24].

Fig. 1 shows an example of a circular deep tunnel excavation with the exterior domain  $\Omega$ , its boundary  $\Gamma$  and some domains  $\Omega_0 \in \Omega$ , where plasticity is assumed to occur.

The boundary integral equation relating the displacements  $\mathbf{u}$  and tractions  $\mathbf{t}$  along the boundary  $\Gamma$  and the initial stresses  $\boldsymbol{\sigma}^0$  in the domain  $\Omega_0$  is [25]:

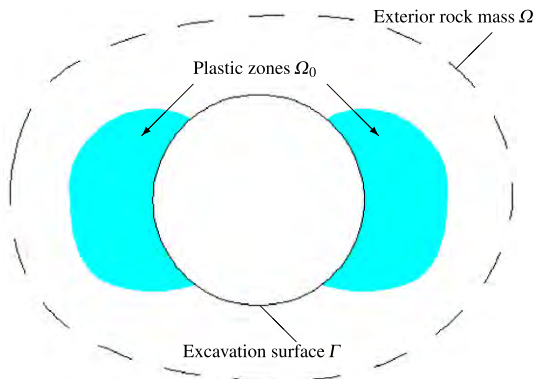


Fig. 1. 2D deep tunnel excavation.

$$\mathbf{C}(P)\mathbf{u}(P) = \int_{\Gamma} \mathbf{U}(P, Q)\mathbf{t}(Q) d\Gamma - \oint_{\Gamma} \mathbf{T}(P, Q)\mathbf{u}(Q) d\Gamma + \int_{\Omega_0} \mathbf{E}(P, \bar{Q})\boldsymbol{\sigma}^0(\bar{Q}) d\Omega_0, \quad (1)$$

where  $P$  and  $Q$  are the source and field points belonging to  $\Gamma$  and where  $\bar{Q}$  represents any point belonging to  $\Omega_0$ .  $\mathbf{C}(P)$  is a matrix containing the free terms which depend on the shape of the boundary near the point  $P$ .  $\mathbf{U}(P, Q)$ ,  $\mathbf{T}(P, Q)$ , and  $\mathbf{E}(P, \bar{Q})$  are matrices containing the fundamental solutions for displacements, tractions, and strains respectively at points  $Q$  and  $\bar{Q}$  due to a unit source at  $P$ .  $\boldsymbol{\sigma}^0$  are the initial stresses related to the nonlinear material behaviour.

In order to solve the boundary value problem illustrated in Fig. 1, the boundary  $\Gamma$  and the domain  $\Omega_0$  are discretised with boundary elements and internal domain cells respectively as shown in Fig. 2.

The discretised form of Eq.(1) is:

$$\mathbf{C}(P)\mathbf{u}(P) = \sum_{e=1}^L \sum_{i=1}^I \mathbf{t}_i^e(Q) \int_{\Gamma^e} \mathbf{U}(P, Q)N_i(Q) d\Gamma_e - \sum_{e=1}^L \sum_{i=1}^I \mathbf{u}_i^e(Q) \oint_{\Gamma^e} \mathbf{T}(P, Q)N_i(Q) d\Gamma_e + \sum_{c=1}^H \sum_{j=1}^h \boldsymbol{\sigma}_j^{0c}(\bar{Q}) \int_{\Omega^c} \mathbf{E}(P, \bar{Q})\hat{N}_j(\bar{Q}) d\Omega_c, \quad (2)$$

where  $N_i(Q)$  and  $\hat{N}_j(\bar{Q})$  are boundary element shape functions and internal domain cell shape functions respectively. In Eq.(2), the outer sums are carried out over the boundary elements or internal domain cells and the inner sums are carried out over the nodes of the boundary elements or internal domain cells. Note that another sum will take place to solve the integrals over the boundary elements  $\Gamma_e$  and the internal domain cells  $\Omega_c$  [7].

Finally, Eq.(2) has to be evaluated for each collocation point  $P_i$  (i.e. each boundary element node) and can be written as:

$$\Delta\mathbf{T}\mathbf{u} = \Delta\mathbf{U}\mathbf{t} + \Delta\mathbf{E}\boldsymbol{\sigma}^0, \quad (3)$$

where  $\mathbf{u}$  is a vector that contains the unknown displacement components,  $\mathbf{t}$  is a vector with traction components of all nodes along the boundary  $\Gamma$  and  $\boldsymbol{\sigma}^0$  is a vector containing the initial stresses at all cell nodes of the domain  $\Omega_0$ .  $\Delta\mathbf{U}$ ,  $\Delta\mathbf{T}$  and  $\Delta\mathbf{E}$  are global coefficient matrices assembled by gathering element or cell contributions.

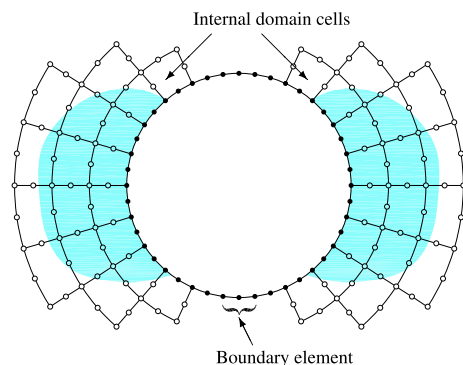


Fig. 2. 2D tunnel excavation discretised with boundary elements and internal domain cells.

### 3. Sequential excavation with the multi-region approach

In order to simulate the staged advance of the excavation process according to the NATM method, multiple boundary element regions which are connected to each other are considered, as shown in Fig. 3.

Various methods for solving multiple region problems exist [3,9]. However, the so called stiffness matrix assembly introduced by Beer [5] is used in this work. The philosophy of this approach is similar to the one used by the FEM. A pseudo stiffness matrix  $\bar{\mathbf{K}}_n^{be}$  of each region  $n$  is computed. The coefficients of this matrix are the tractions due to unit displacements. The matrices  $\bar{\mathbf{K}}_n^{be}$  of all regions are then assembled in the same way as in the FEM. An advantage of this method, specially for this work, is that it can also be used for coupling boundary elements with finite elements.

Both the displacements  $\mathbf{u}$  and the tractions  $\mathbf{t}$  are unknown at the interfaces between the regions. Therefore, the number of unknowns is increased and additional equations are needed. These equations can be obtained from the condition of equilibrium and compatibility at the interfaces of the regions.

To obtain the pseudo stiffness matrix  $\bar{\mathbf{K}}_n^{be}$  of a region, a pure Dirichlet problem using Eq.(3) (with  $\sigma^0 = 0$ ) has to be solved  $M$  times, where  $M$  is the number of degrees of freedom (DoF) of the boundary element region. The coefficients of  $\bar{\mathbf{K}}_n^{be}$  are such that:

$$\mathbf{t}_n = \bar{\mathbf{K}}_n^{be} \mathbf{u}_n. \tag{4}$$

The stiffness matrices  $\bar{\mathbf{K}}_n^{be}$  of each region are assembled into the global system of equation, which then can be solved for the unknown displacements at the interfaces.

As it can be seen in Fig. 3, only some of the nodes of region 0 are connected to region 2 or region 3. It would obviously be more efficient to consider only the interface nodes, i.e. only those nodes that are connected to a region, in the calculation of the pseudo stiffness matrix. The procedure is, therefore, first to solve the problem with zero values of  $\mathbf{u}$  at the interfaces between regions, and secondly, to solve the problem where unit values of  $\mathbf{u}$  are applied at each node in turn.

For the complete solution of the partially coupled problem shown in Fig. 3 four steps have to be executed [12,7]:

- (a) The problem is solved for the boundary conditions applied at the nodes which are not connected to other regions (free nodes) (see Fig. 3) with the interface nodes fixed so that the traction at the interfaces (coupled nodes)  $\mathbf{t}_{c0n}$  is obtained. According to that, the following system of equation can be written to each region  $n$ :

$$[\mathbf{A}_n] \begin{Bmatrix} \mathbf{t}_{c0n} \\ \mathbf{u}_{f0n} \end{Bmatrix} = \{\mathbf{F}_{0n}\}, \tag{5}$$

where  $\mathbf{A}_n$  is the assembled left-hand side,  $\mathbf{F}_{0n}$  is the right hand side due to given boundary conditions, which are the tractions at the free nodes and  $\mathbf{u}_{f0n}$  contains the displacements at the free nodes.

- (b) The pseudo stiffness matrix  $\bar{\mathbf{K}}_n^{be}$  of each region is computed for the interface nodes by solving the following system of equation:

$$[\mathbf{A}_n] \begin{Bmatrix} \mathbf{t}_{c_n} \\ \mathbf{u}_{f_n} \end{Bmatrix} = \{\mathbf{F}_n\}, \tag{6}$$

where  $\mathbf{F}_n$  is the right-hand side computed for a unit value of  $\mathbf{u}$  applied at  $x$ ,  $y$  or  $z$ -direction at the interface nodes. The vector  $\mathbf{t}_{c_n}$  contains the tractions at the coupled nodes and  $\mathbf{u}_{f_n}$  the displacements at the free nodes. Note that  $\mathbf{A}_n$  on the left hand side of Eq.(6) is the same as in Eq.(5). Thus, the first and second problem can be solved in one step with a multiple right hand side solver. As a result,

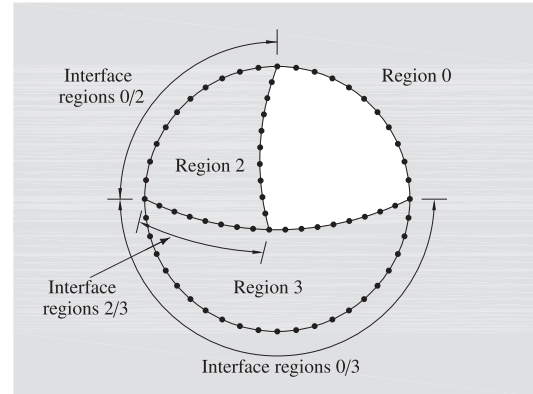


Fig. 3. Partially coupled problem – staged tunnel excavation with top heading and bench discretised with multiple boundary element regions.

the pseudo stiffness matrix  $\bar{\mathbf{K}}_n^{be}$  for the interface of each boundary element region is obtained as:

$$\bar{\mathbf{K}}_n^{be} = \begin{bmatrix} \mathbf{t}_{c_n}^1 & \mathbf{t}_{c_n}^2 & \dots & \mathbf{t}_{c_n}^{\hat{M}} \end{bmatrix}, \tag{7}$$

where  $\hat{M}$  is the number of DoF of the interface nodes.

- (c) By using the conditions for equilibrium and compatibility at the interface, the pseudo stiffness matrices  $\bar{\mathbf{K}}_n^{be}$  of each region  $n$  are assembled into the global system of equation, which then can be solved for the unknown displacements  $\mathbf{u}_c$  at the interfaces as follows:

$$[\bar{\mathbf{K}}^{be}] \{\mathbf{u}_c\} = \{\mathbf{F}\}, \tag{8}$$

where  $\bar{\mathbf{K}}^{be}$  is the assembled “pseudo stiffness matrix” of the interface nodes and  $\mathbf{F}$  is the assembled right-hand side.

- (d) After the interface unknowns have been determined, the results at the interface are used to compute the remaining unknowns of all regions by using

$$\begin{Bmatrix} \mathbf{t}_{c_n} \\ \mathbf{x}_{f_n} \end{Bmatrix} = \begin{Bmatrix} \mathbf{t}_{c0n} \\ \mathbf{x}_{f0n} \end{Bmatrix} + \begin{bmatrix} \bar{\mathbf{K}}_n^{be} \\ \mathbf{Y}_n \end{bmatrix} \{\mathbf{u}_{c_n}\} \tag{9}$$

in which  $\mathbf{Y}_n$  is defined as:

$$\mathbf{Y}_n = \begin{bmatrix} \mathbf{u}_{f_n}^1 & \mathbf{u}_{f_n}^2 & \dots & \mathbf{u}_{f_n}^{\hat{M}} \end{bmatrix} \tag{10}$$

and the vector  $\mathbf{u}_{c_n}$  is obtained by gathering values from the vector of unknowns at all the interface nodes  $\mathbf{u}_c$ .

### 4. Simulation of ground support

#### 4.1. Shotcrete as an assembly of shell finite elements

For the shotcrete simulation, a simple and efficient curved shell finite element formulation [1,4,30] degenerated from a 3D isoparametric finite element is used and Reissner–Mindlin theory is assumed. The advantage of this formulation is that it is applicable to moderately thick shells and that the edges do not have to be normal to the shell surface (an advantage when dealing with an increase in thickness at the bottom of the shotcrete shell also known as “elephant feet”).

The shell geometry (Fig. 4) and its displacement field (Fig. 5) can be described as:

$$\mathbf{x} = \begin{Bmatrix} x \\ y \\ z \end{Bmatrix} = \sum_{i=1}^l \bar{N}_i(\xi, \eta) \left( \begin{Bmatrix} x_i \\ y_i \\ z_i \end{Bmatrix} + \zeta \begin{Bmatrix} t_{xi} \\ t_{yi} \\ t_{zi} \end{Bmatrix} \right) \tag{11}$$

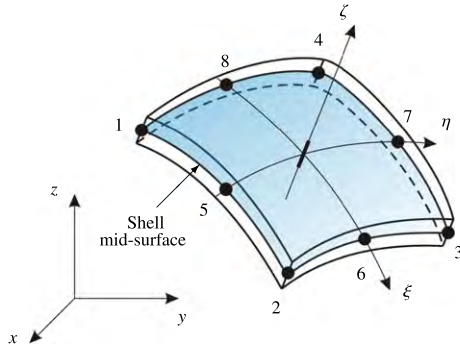


Fig. 4. General 8-node curved shell finite element used for the simulation of the shotcrete.

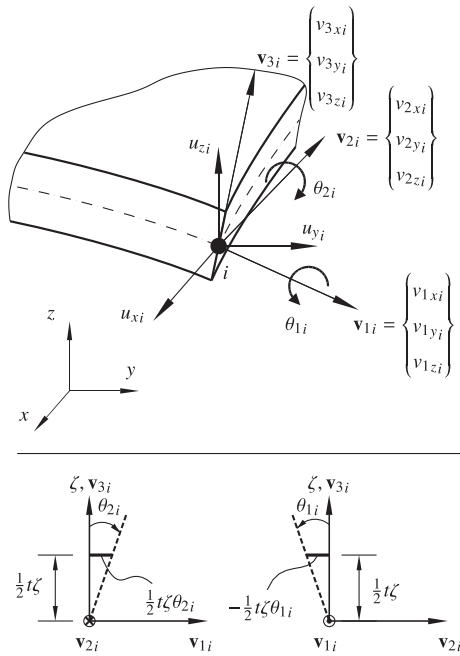


Fig. 5. Shell element nodal DoF ( $u_{xi}, u_{yi}, u_{zi}, \theta_{1i}, \theta_{2i}$ ) and orthogonal unit vectors  $\mathbf{v}_{1i}, \mathbf{v}_{2i}$  and  $\mathbf{v}_{3i}$ .

and

$$\mathbf{u} = \begin{Bmatrix} u_x \\ u_y \\ u_z \end{Bmatrix} = \sum_{i=1}^l \bar{N}_i(\xi, \eta) \left( \begin{Bmatrix} u_{xi} \\ u_{yi} \\ u_{zi} \end{Bmatrix} + \frac{1}{2} t \zeta \begin{Bmatrix} \theta_{2i} v_{1xi} - \theta_{1i} v_{2xi} \\ \theta_{2i} v_{1yi} - \theta_{1i} v_{2yi} \\ \theta_{2i} v_{1zi} - \theta_{1i} v_{2zi} \end{Bmatrix} \right) \quad (12)$$

respectively, where  $t$  is the element thickness,  $\mathbf{v}_{1i}, \mathbf{v}_{2i}$  and  $\mathbf{v}_{3i}$  are local, orthogonal unit vectors at the element node  $i$  as shown in Fig. 5.  $\bar{N}_i(\xi, \eta)$  are the shape functions of an isoparametric finite shell element and  $l$  indicates the number of nodes which corresponds to the number of nodes of the boundary elements. The thickness vector  $\mathbf{t}_i$  is given by:

$$\mathbf{t}_i = \frac{1}{2} t \mathbf{v}_{3i}. \quad (13)$$

Note that in Eq.(12) the nodal displacements  $u_{xi}, u_{yi}$  and  $u_{zi}$  are defined globally while the nodal rotations  $\theta_{1i}$  and  $\theta_{2i}$  are defined locally as shown in Fig. 5.

By using Eqs.(11) – (12), the stiffness matrix of the shell element (computed for its mid-surface) can be obtained by:

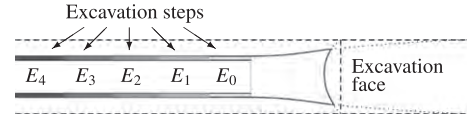


Fig. 6. Modeling the evolution of the shotcrete strength properties according to the excavation steps.

$$\mathbf{K}^{fe} = \int_{\Omega_e} \mathbf{B}^T \mathbf{D} \mathbf{B} d\Omega_e, \quad (14)$$

where  $\mathbf{B}$  is the strain–displacement matrix, which contains derivatives of the shape functions  $\bar{N}_i(\xi, \eta)$  and  $\mathbf{D}$  is the constitutive matrix employed in the formulation, which is defined as:

$$\mathbf{D} = \frac{E}{(1 - \nu^2)} \begin{bmatrix} 1 & \nu & 0 & 0 & 0 \\ \nu & 1 & 0 & 0 & 0 \\ 0 & 0 & \frac{(1-\nu)}{2} \kappa & 0 & 0 \\ 0 & 0 & 0 & \frac{(1-\nu)}{2} \kappa & 0 \\ 0 & 0 & 0 & 0 & \frac{(1-\nu)}{2} \kappa \end{bmatrix}, \quad (15)$$

where  $\nu$  and  $E$  are the Poisson’s ratio and the Young’s modulus respectively, and  $\kappa$  is the shear correction factor (e.g.  $\kappa = \frac{5}{6}$  for homogeneous rectangular cross-section).

#### 4.1.1. Consideration of the hydration process

In order to have an accurate and realistic simulation of the shotcrete support, the change in the shotcrete strength due to hydration needs to be taken into consideration. This is done by changing the stiffness properties of the shell elements during the analysis process (Fig. 6) by a new developed approach [19] that makes use of a series of look-up tables. These tables provide isotropic elastic stiffness and strength data (Young’s modulus  $E$ , Poisson’s ratio  $\nu$  and uniaxial compressive strength  $f_{cu}$ ) of hydrating shotcrete dependent on the time of application of the shotcrete (degree of hydration), its water–cement ratio  $w/c$  and its aggregate–cement ratio  $a/c$ .

#### 4.1.2. Look-up tables

The values in the look-up tables depend basically on the hydration  $\bar{\xi}(t)$ , where  $t$  is the time passed since the application of the shotcrete, and the shotcrete composition in terms of water–cement ratio  $w/c$  and aggregate–cement ratio  $a/c$ .

According to Scheiner et al. [19], the hydration degree–time relationship can be computed by means of numerical integration of the following macroscopic Arrhenius-type reaction kinetics law:

$$\bar{\xi}(t) = \int_{\tau}^t \tilde{A}[\bar{\xi}(\tau)] \exp\left(-\frac{E_a}{RT(\tau)}\right) d\tau. \quad (16)$$

$\tilde{A}[\bar{\xi}(\tau)]$  is the macroscopic shotcrete-specific chemical affinity that describes the hydration kinetics,  $E_a$  is the activation energy,  $R$  is the universal gas constant and  $T(\tau)$  is the history of absolute temperature in the sample.

In this work the following relationship is used:

$$\tilde{A}(\bar{\xi}) = \begin{cases} \frac{a[1-\exp(-b\bar{\xi})]}{1+c\bar{\xi}^d} & \text{if } \bar{\xi} \leq e \\ \frac{a[1-\exp(-b\bar{\xi})]}{1+c\bar{\xi}^d} & \text{if } \bar{\xi} \geq e \end{cases} \quad (17)$$

with  $a = 7.313 \text{ s}^{-1}$ ,  $b = 10.46$ ,  $c = 169.3$ ,  $d = 4.37$ ,  $e = 0.05$  and the ratio between activation energy and universal gas constant  $E_a/R = 4000 \text{ K}$ .

The look-up tables which provide the properties of hydrating shotcrete for “sealed conditions” and for “drained conditions” for a water–cement ratio of  $w/c = 0.4$  are represented in Figs. 7 and 8. Blue curves refer to sealed conditions, while black curves refer

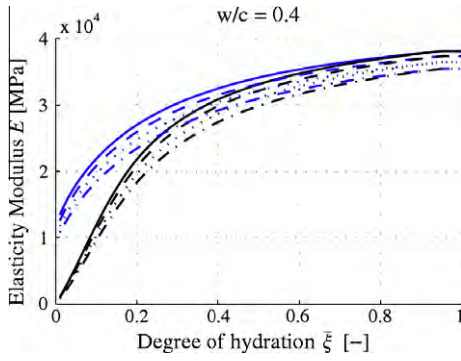


Fig. 7. Look-up tables for Young's modulus  $E$  [19].

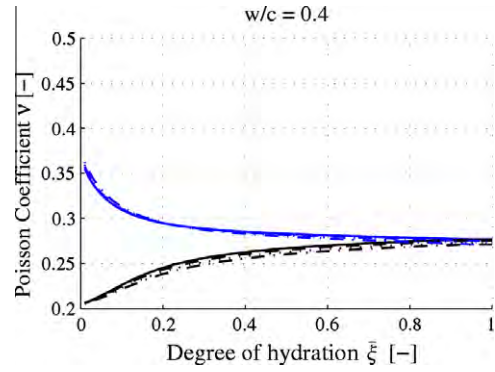


Fig. 8. Look-up tables for Poisson's ratio  $\nu$  [19].

to drained conditions. Solid curves refer to  $a/c = 5.0$ , dashed curves to  $a/c = 4.5$ , dotted curves to  $a/c = 4.0$ , and dash-dotted curves to  $a/c = 3.5$ . Sealed conditions apply when no water can escape from the cement paste matrix under loading conditions. If the water pressure is equal to the pressure of the air within the tunnel, i.e. the water pressure is controlled from outside the tunnel shell, then drained conditions apply. If there is any doubt, Scheiner et al. [19] recommend to use the data related to sealed conditions.

The time of hydration  $t$  is simulated by the number of excavation steps that have occurred since the installation of the shotcrete times the time of the advance of the tunnel face as indicated in Fig. 6. The relationship between the hydration degree  $\xi$  and the time  $t$  after spraying is computed by using Eq.(16).

4.2. Steel arches as an assembly of beam finite elements

The curved beam element for the simulation of the steel arch supports is formulated in an analogous way to the formulation of the curved shell element. The basic kinematic assumptions are the assumptions of the Timoshenko beam theory.

The geometry of the element (Fig. 9) and its displacement field (Fig. 10) is defined by:

$$\mathbf{x} = \begin{Bmatrix} x \\ y \\ z \end{Bmatrix} = \sum_{i=1}^g \tilde{N}_i(\xi) \left( \begin{Bmatrix} x_i \\ y_i \\ z_i \end{Bmatrix} + \eta \begin{Bmatrix} b_{xi} \\ b_{yi} \\ b_{zi} \end{Bmatrix} + \zeta \begin{Bmatrix} h_{xi} \\ h_{yi} \\ h_{zi} \end{Bmatrix} \right) \quad (18)$$

and

$$\mathbf{u} = \begin{Bmatrix} u_x \\ u_y \\ u_z \end{Bmatrix} = \sum_{i=1}^g \tilde{N}_i(\xi) \left( \begin{Bmatrix} u_{xi} \\ u_{yi} \\ u_{zi} \end{Bmatrix} + \frac{1}{2} b \eta \begin{Bmatrix} \theta_{1i} v_{3xi} - \theta_{3i} v_{1xi} \\ \theta_{1i} v_{3yi} - \theta_{3i} v_{1yi} \\ \theta_{1i} v_{3zi} - \theta_{3i} v_{1zi} \end{Bmatrix} - \frac{1}{2} h \zeta \begin{Bmatrix} \theta_{2i} v_{1xi} + \theta_{1i} v_{2xi} \\ \theta_{2i} v_{1yi} + \theta_{1i} v_{2yi} \\ \theta_{2i} v_{1zi} + \theta_{1i} v_{2zi} \end{Bmatrix} \right) \quad (19)$$

respectively, where  $\mathbf{b}_i = \frac{1}{2} b \mathbf{v}_{2i}$  is the width vector,  $\mathbf{h}_i = \frac{1}{2} h \mathbf{v}_{3i}$  is the height vector, and  $\mathbf{v}_{1i}$ ,  $\mathbf{v}_{2i}$  and  $\mathbf{v}_{3i}$  are local orthogonal unit vectors at the element node  $i$  as shown in Fig. 10.  $\tilde{N}_i(\xi)$  are quadratic shape functions of an isoparametric one-dimensional beam finite element and the natural coordinates  $(\xi, \eta, \zeta)$  vary between  $-1$  and  $1$  on the respective faces of the element.

Note that, for simplicity, the cross-section of the element in Fig. 9 is rectangular and constant throughout the element length. However, any cross-section can be considered by a suitable modification of the input parameters.

For the evaluation of the strain–displacement matrix  $\mathbf{B}$ , only the strain components in longitudinal direction  $\epsilon_{\xi\xi}$  and in transversal shear directions  $\epsilon_{\xi\eta}$  and  $\epsilon_{\xi\zeta}$  are of interest. Thus,

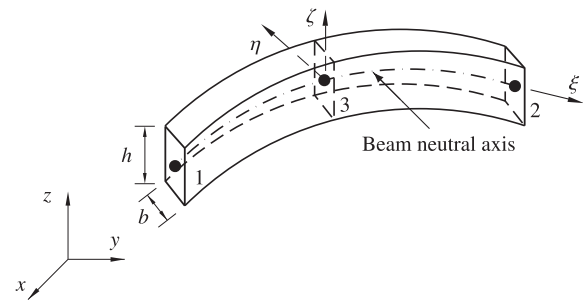


Fig. 9. General 3-node curved beam finite element used for the simulation of the steel arches.

$$\boldsymbol{\epsilon} = \begin{Bmatrix} \epsilon_{\xi\xi} \\ \epsilon_{\xi\eta} \\ \epsilon_{\xi\zeta} \end{Bmatrix} = [\mathbf{B}_1 \quad \mathbf{B}_2 \quad \mathbf{B}_3] \begin{Bmatrix} \bar{\mathbf{u}}_1 \\ \bar{\mathbf{u}}_2 \\ \bar{\mathbf{u}}_3 \end{Bmatrix} = \mathbf{B}\bar{\mathbf{u}}, \quad (20)$$

where the local axes  $\xi$ ,  $\eta$  and  $\zeta$  are assumed to be orthogonal.

The corresponding stress–strain law to be employed in the formulation is:

$$\begin{Bmatrix} \sigma_{\xi\xi} \\ \sigma_{\xi\eta} \\ \sigma_{\xi\zeta} \end{Bmatrix} = \begin{bmatrix} E & 0 & 0 \\ 0 & \kappa G & 0 \\ 0 & 0 & \kappa G \end{bmatrix} \begin{Bmatrix} \epsilon_{\xi\xi} \\ \epsilon_{\xi\eta} \\ \epsilon_{\xi\zeta} \end{Bmatrix}, \quad (21)$$

where  $E$  is the Young's modulus,  $G$  is the shear modulus and  $\kappa$  the shear correction factor of the steel arch.

4.2.1. Consideration of yielding connections

The simulation of special yielding joints [2,16] in the steel arches as shown in Fig. 11 is achieved with the use of a yield function  $F$  posing a limit to the axial forces acting on the element. The yield function is

$$F = N - \mu C, \quad (22)$$

where  $N$  is the axial force on the beam element,  $\mu$  is the static friction coefficient and  $C$  is the clamping force acting on the yielding joint.

5. General coupling strategy for ground/support interaction

In order to consider the shotcrete and steel arch supports in the sequential excavation process, the stiffness matrices of the shell and beam finite elements need to be assembled into the global interface stiffness matrix which consists of the assembled contributions of all interface stiffness matrices of the boundary element regions.

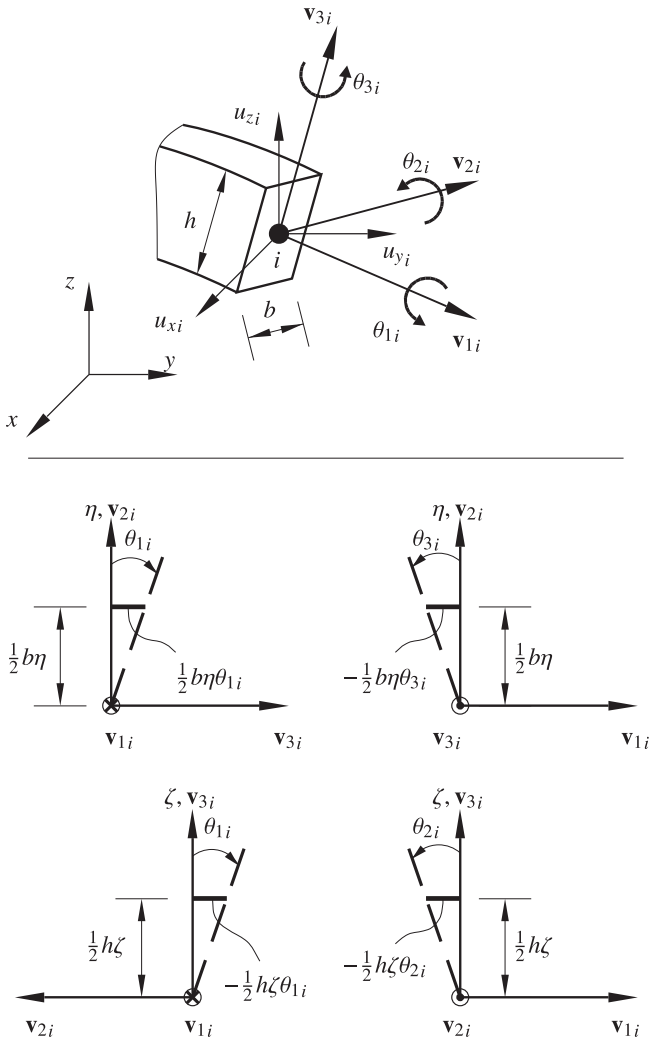


Fig. 10. Beam element nodal DoF ( $u_{xi}, u_{yi}, u_{zi}, \theta_{1i}, \theta_{2i}, \theta_{3i}$ ) and orthogonal unit vectors  $\mathbf{v}_{1i}$ ,  $\mathbf{v}_{2i}$  and  $\mathbf{v}_{3i}$ .

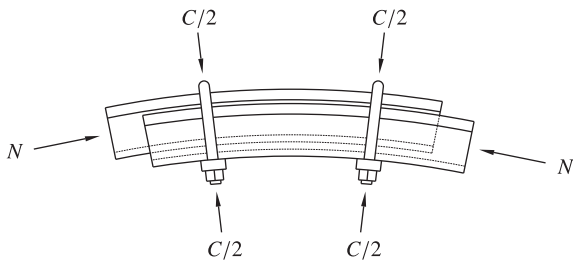


Fig. 11. Clamping and normal forces on a yielding joint.

The boundary element pseudo stiffness matrix  $\bar{\mathbf{K}}_n^{be}$  in Eq.(4) relates nodal displacements to nodal tractions. Therefore, it must be converted into a real stiffness matrix (in the FEM sense). This is done by converting the nodal tractions in Eq.(4) into nodal point forces as proposed by Beer and Watson [8] with

$$\mathbf{F} = \mathbf{M}\mathbf{t}, \quad (23)$$

where the coefficients of the matrix  $\mathbf{M}$  are

$$M_{ij} = \int_{\Gamma_e} G_i G_j d\Gamma_e \quad (24)$$

with  $G_i$  and  $G_j$  being globally defined basis functions.

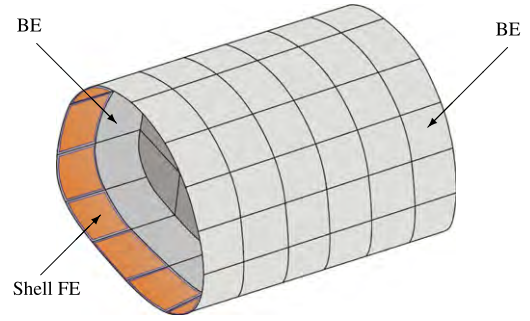


Fig. 12. Sketch of shell finite elements (FE) and boundary elements (BE).

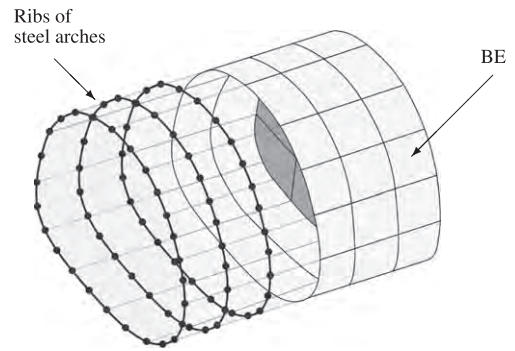


Fig. 13. Sketch of beam finite elements (FE) and boundary elements (BE).

Hence, according to Eq.(23) and Eq.(4), the interface stiffness matrix of the boundary element region  $n$  can be obtained as:

$$\mathbf{K}_n^{be} = \mathbf{M}_n \bar{\mathbf{K}}_n^{be}. \quad (25)$$

Now, the stiffness matrices of the boundary element region  $\mathbf{K}_n^{be}$  and finite element regions  $\mathbf{K}_n^{fe}$  can be assembled exactly as in a standard finite element analysis. Note that  $\mathbf{K}_n^{be}$  is not symmetric whereas  $\mathbf{K}_n^{fe}$  is symmetric.

Finally, two assumptions regarding the coupling of the boundary elements to shell and/or beam finite elements are made. Firstly, the eccentricity between the shell mid-surface nodes (and also the beam neutral axis) and the boundary element nodes is considered as negligible. Secondly, the difference in the numbers of DoF between the boundary element (3 translations and 2 rotations) and the shell finite element (3 translations and 3 rotations) is dealt with in such a way that only the corresponding DoF are added (i.e. no rotational DoF of the finite elements contribute to the translational ones of the boundary elements). The second assumption follows from the first one, i.e. rotations do not have any effect on the interface displacements. As a result, the nodes of the shell and also the beam elements have the same coordinates as the nodes of the boundary elements as shown in Figs. 12 and 13. This makes mesh generation very easy since all elements are considered to be on the same surface.

## 6. Simulation of nonlinear ground behaviour

In nonlinear analysis, the displacements and tractions depend on the deformation history, and therefore, incremental quantities denoted by overdots are used. Hence, Eq.(1) becomes

$$\mathbf{C}(P)\dot{\mathbf{u}}(P) = \int_{\Gamma} \mathbf{U}(P, Q)\dot{\mathbf{t}}(Q)d\Gamma - \int_{\Gamma} \mathbf{T}(P, Q)\dot{\mathbf{u}}(Q)d\Gamma + \int_{\Omega_0} \mathbf{E}(P, \bar{Q})\dot{\sigma}^0(\bar{Q})d\Omega_0. \quad (26)$$

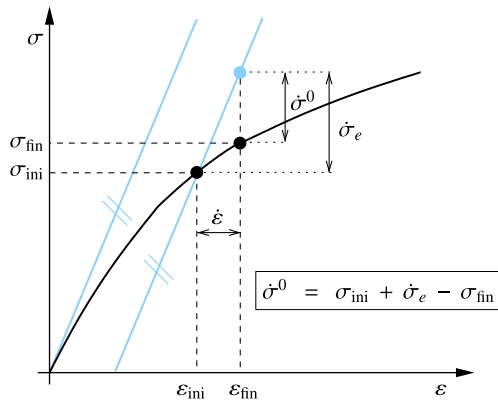


Fig. 14. Schematic illustration for the computation of the initial stress  $\sigma^0$ .

The following equation is used for the evaluation of the stress increments at an internal point  $\bar{P}$  [25]:

$$\begin{aligned} \dot{\sigma}(\bar{P}) = & \int_{\Gamma} \mathbf{D}(\bar{P}, Q) \dot{\mathbf{t}}(Q) d\Gamma - \oint_{\Gamma} \mathbf{S}(\bar{P}, Q) \dot{\mathbf{u}}(Q) d\Gamma \\ & + \int_{\Omega_0} \mathbf{W}(\bar{P}, Q) \dot{\sigma}^0(Q) d\Omega_0 + \mathbf{F} \dot{\sigma}^0(\bar{P}). \end{aligned} \quad (27)$$

The initial stresses  $\sigma^0$  are calculated from the non linear stress-strain relationship of the material. In principle, this procedure consists of two steps [21]: the elastic predictor and the plastic corrector. In the first step, the problem is solved by assuming that the material is purely elastic within the interval considered. In the second step, the influence of the plastic flow is taken into account and the final stress state  $\sigma_{ij}^{fin}$  which lies on or inside the yield surface is computed if the elastic trial state violates the yield condition. A schematic illustration for the computation of the initial stress is shown in Fig. 14.

6.1. Rock behaviour – hierarchical constitutive model

The hyperbolic Mohr–Coulomb model (HMCM) proposed by Gens et al. [14] is adopted in this work. The HMCM is a hierarchical constitutive model with linear elastic and strain hardening/softening plastic behaviour and three different flow rules. The HMCM yield surface is described by a hyperbolic yield function that tends asymptotically to the linear Mohr–Coulomb model in the  $p - \sqrt{J_2}$ -plane (Fig. 15), where  $p$  indicates the mean stress defined by  $p = \frac{1}{3}$  with  $I_1$  being the first invariant of the stress tensor and  $J_2$  indicates the second invariant of the deviatoric stress tensor.

As shown in Fig. 16, the HMCM represents a variety of yield surfaces on the  $\pi$ -plane according to the following equations:

$$F = J_2 - F_1(p, h_\nu) F_2(\theta) \quad (28a)$$

$$F_1(p, h_\nu(\tan \phi, C)) = (C + p \tan \phi)^2 - (C - p_t \tan \phi)^2 \quad (28b)$$

$$F_2(\theta) = (1 + Y \sin(3\theta))^2 \quad (YZ \geq 0; -1 \leq Y \leq 1), \quad (28c)$$

where  $p_t$  is the triaxial tensile strength,  $h_\nu(\tan \phi, C)$  is the history variable,  $C$  is the apparent cohesion,  $\tan \phi$  is the slope of the conical surface,  $\theta$  is the Lode angle and  $Y$  and  $Z$  are parameters that shape the trace of the yield surface on the deviatoric plane. Note that Eq.(28b) accounts for the shape of the curve shown in Fig. 15, while Eq.(28c) accounts for the shape of the curve shown in Fig. 16.

In Fig. 15, compressive stresses are assumed as positive and the parameter  $\hat{q}$  is the tension limit predicted by the linear Mohr–Coulomb model.

Different yield surfaces are represented in Fig. 16. They can be achieved by simply changing the values given to the parameters  $Y$  and  $Z$  in Eq.(28c). For instance, the deviatoric cross-section

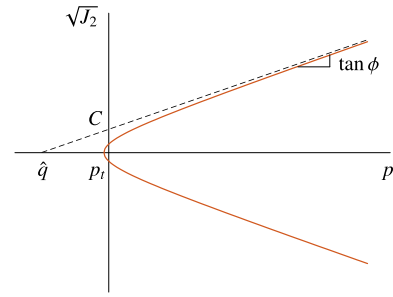


Fig. 15. Trace of the yield surface of the HMCM on the  $p - \sqrt{J_2}$ -plane.

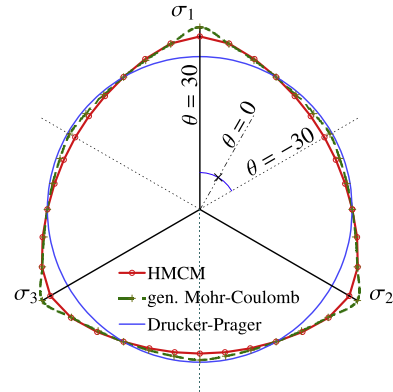


Fig. 16. Traces of the HMCM yield surface on the  $\pi$ -plane.

becomes a circle corresponding to a Drucker–Prager yield surface for  $Y = 0$  and  $Z = 0$ . The hyperbolic Mohr–Coulomb yield surface is approached by using  $Y = -0.85 \sqrt{\sin(\phi)}$  and  $Z = -0.229$ . The influence of the hydrostatic stress  $p$  and the shape of the yield surface on the  $p - \sqrt{J_2}$ -plane (Fig. 15) are defined by Eq.(28b), whereas the influence of the Lode angle  $\theta$  and the shape of the yield surface on the deviatoric plane-(Fig. 16) are defined by Eq.(28c).

6.1.1. The flow rule

Three different flow rules are considered in the HMCM: one associated flow rule with  $Q = F$  and two non-associated flow rules. The non-associated flow rules are restricted to the volumetric component only with the purpose of reducing volumetric dilatancy for high compressive confinements.

The derivatives of the plastic potential  $m_{ij}$  in respect to the invariants  $p, J$ , and  $\theta$  are defined as:

$$m_{ij} = \frac{\partial Q}{\partial \sigma_{ij}} = \frac{\partial Q}{\partial p} \frac{\partial p}{\partial \sigma_{ij}} + \frac{\partial Q}{\partial J} \frac{\partial J}{\partial \sigma_{ij}} + \frac{\partial Q}{\partial \theta} \frac{\partial \theta}{\partial \sigma_{ij}}. \quad (29)$$

The derivatives of the plastic potential with respect to  $J$  and  $\theta$  are not depending on the flow rule because associativity is assumed for these components. They become:

$$\frac{\partial Q}{\partial J} = 2J \quad (30)$$

and

$$\frac{\partial Q}{\partial \theta} = -3YZF_1 \cos(3\theta)(1 + Y \sin(3\theta))^{Z-1}. \quad (31)$$

However, the derivative of the plastic potential with respect to  $p$  is different for each of the three flow rules considered:

(a) Associated flow rule:

$$\frac{\partial Q}{\partial p} = -3 \tan \phi (C + p \tan \phi)(1 + Y \sin(3\theta))^Z \quad (32)$$

(b) "Standard" non-associated flow rule with a pressure-dependent decay function:

$$\frac{\partial Q}{\partial p} = -2f_m(p) \tan \phi (C + p \tan \phi) (1 + Y \sin(3\theta))^2 \quad (33)$$

In this flow rule the most common type of non-associativity is followed. A decay function  $f_m(p)$  defined by:

$$f_m(p) = \begin{cases} 1 & p < 0 \\ \frac{1}{2} \left[ 1 + \cos \left( \pi \frac{p}{p_{nodil}} \right) \right] & 0 \leq p \leq p_{nodil} \\ 0 & p > p_{nodil} \end{cases} \quad (34)$$

decreases with increasing pressure, and therefore, it reduces the volumetric component. It is defined in such a way that the resulting flow rule satisfies the following requirements [14]:

- Only volumetric deformations occur for triaxial tension loading. In other words, the flow rule at the tip of the hyperbola must be parallel to the  $p$  axis. This is achieved if  $f_m(p) = 1$ .
- The dilatancy effect is almost negligible for high compressive confinement. So, the flow rule must be orthogonal to the  $p$  axis for values higher than a certain threshold level given as the parameter  $p_{nodil}$ . This requires that  $f_m(p_{nodil}) = 0$ .

In Fig. 17 the directions of the flow rule in the main loading situations are shown together with the projection of the yield surface on to the  $J - p$ -plane. The direction of the derivatives of the plastic potential does not necessarily follow the radial direction, i.e. straight line from the origin, except for the stress point tip of the hyperbola although Fig. 17 may give that impression.

(c) "Radial" non-associated flow rule with decay function:

$$\frac{\partial Q}{\partial p} = -2f_m|p| \quad (35)$$

In this case the decay function  $f_m(p)$  is defined by:

$$f_m(p) = \begin{cases} 1 & p + \frac{J}{\sqrt{3}} < 0 \\ \frac{1}{2} \left[ 1 + \cos \left( \pi \frac{p + \frac{J}{\sqrt{3}}}{p_{nodil}} \right) \right] & 0 \leq p + \frac{J}{\sqrt{3}} \leq p_{nodil} \\ 0 & p + \frac{J}{\sqrt{3}} > p_{nodil} \end{cases} \quad (36)$$

This flow rule considers that for some materials under monotonic uniaxial tension the flow rule should only produce plastic deformations in the direction of the loading. This is equivalent to stating that the micro-cracks opened under uniaxial tension should be perpendicular to the loading direction. Note that the function in Fig. 18 gives no reduction of

dilatancy between the hyperbola tip and the uniaxial tension point on the hyperbola (point on a straight line with slope  $J = \sqrt{3}|p|$ ). There is also a progressive decline of dilatancy from that point to the right.

### 6.1.2. Evolution law and history variable

The history variable  $H_v$  is the accumulated deviatoric plastic strain defined as:

$$H_v = \Delta\lambda \sqrt{m_{ij}^D m_{ij}^D}, \quad (37)$$

where  $m_{ij}^D$  are the deviatoric components of the derivatives of the plastic potential and  $\Delta\lambda$  indicates the plastic multiplier.

The evolution of the yield surface is controlled by the evolution of each of the parameters  $p_r$ ,  $C$  and  $\tan\phi$  in terms of the history variable. For that purpose, a function is used which consists of three different parts: initial hardening, softening and final residual. Hardening and softening sections are controlled by a cosine-based function  $f^*(H_v)$  which is defined as

$$f^*(H_v) = \begin{cases} f_0 & H_v = 0 \\ f_0 + (f_p - f_0) \cos \left( \frac{\pi}{2} (S(\beta_H, \alpha_H) + 3) \right) & 0 \leq H_v \leq H_{vp} \\ f_r + (f_p - f_r) \frac{1}{2} [\cos(\pi S(\beta_S, \alpha_S)) + 1] & H_{vp} \leq H_v \leq H_{vr} \\ f_r & H_v > H_{vr}, \end{cases} \quad (38)$$

where  $f_0$  is the tension limit, cohesion or internal friction angle at the initial yield state,  $f_p$  is the tension limit, cohesion or internal friction angle at peak, and  $f_r$  is the residual tension limit, cohesion or internal friction angle of the rock. The function  $S(\beta, \alpha)$  is defined as:

$$S(\beta_i, \alpha_i) = \frac{e^{-\alpha_i} \beta_i}{1 + (e^{-\alpha_i} - 1) \beta_i} \quad (39)$$

with

$$(\beta_i, \alpha_i) = \begin{cases} \beta_i = \beta_H = \frac{H_v}{H_{vp}} & \alpha_i = \alpha_H, 0 \leq H_v \leq H_{vp} \\ \beta_i = \beta_S = \frac{H_v - H_{vp}}{H_{vr} - H_{vp}} & \alpha_i = \alpha_S, H_{vp} \leq H_v \leq H_{vr}, \end{cases} \quad (40)$$

in which  $\alpha_i$  is a "shape" coefficient, which may have different values for the hardening section  $\alpha_H$  and the softening section of the diagram  $\alpha_S$ , leading to a family of possible evolution laws in which hardening or softening for each parameter may evolve faster at the beginning or at the end of the inelastic process. The effect of those parameters on the evolution laws can be seen in Fig. 19.

Note that for  $\alpha_i = 0$  one obtains  $S = \zeta_i$  from Eq.(39) and the original form of evolution laws without scaling functions is obtained as it can be seen from Fig. 19. This means that in general the parameters  $\alpha_i$  can be assigned equal to zero, unless required for specific data fitting.

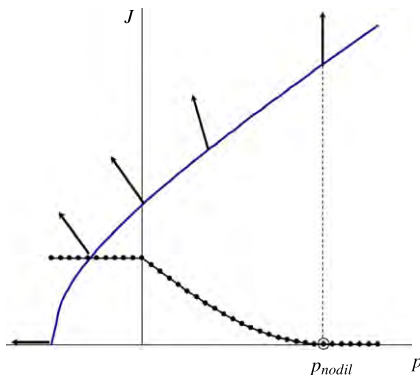


Fig. 17. "Standard" non-associated flow rule with a pressure-dependent decay function [14].

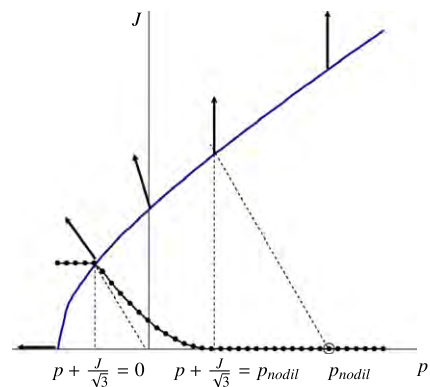


Fig. 18. "Radial" non-associated flow rule [14].

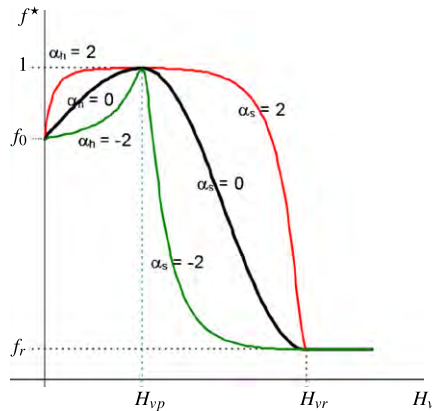


Fig. 19. Influence of the effect of the parameters  $\alpha_i$  on the family of evolution laws [14].

7. Examples

7.1. Circular excavation without support

To demonstrate the efficiency and accuracy of the implemented boundary element approach for nonlinear analysis, a circular tunnel with a diameter of 12 m in a virgin stress field of  $\sigma_y = -54$  MPa,  $\sigma_x = \sigma_z = 0.5\sigma_y$  is analysed. The tunnel is excavated in one step and no support is considered. Both plane strain and 3D analyses are carried out. The results for the 3D mesh are obtained for a section that is far enough away from the tunnel face so that plane strain conditions prevail.

The nonlinear analysis is carried out with the use of the HMCM with associated flow rule for the material parameters shown in Table 1.

The boundary element and internal domain cell discretisation used for the analyses with the BEM is shown in Fig. 20. The results of the FEM analysis are obtained with a mesh at least twice as fine as the boundary element mesh.

The results for radial and tangential stress for a horizontal line normal to the tunnel axis are shown in Fig. 21, where 2D and 3D results of the presented work are compared to a 2D finite element analysis carried out with Plaxis.

7.2. Influence of the tunnel lining

In this example, a series of nonlinear analyses with different support conditions is carried out for a sequential circular excavation with 12 m diameter shown in Fig. 22. The virgin stress field considered is  $\sigma_{zz} = -2.75$  MPa,  $\sigma_{xx} = \sigma_{yy} = 0.5\sigma_{zz}$ . The constitutive model used is the HMCM with associated flow rule. The material properties are shown in Table 2.

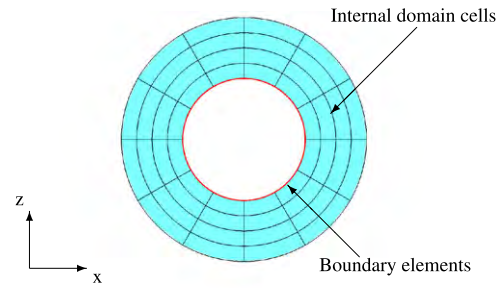
For the shotcrete simulation, two conditions are considered: drained condition, in which the shotcrete hydration takes place slowly, and sealed condition, in which the shotcrete hydration takes place faster. The shotcrete material properties are taken from the look-up tables shown in Section 4.1.2 with  $w/c = 0.4$  and  $a/c = 3.5$ . The shotcrete thickness considered in the analysis is 35 cm.

For the steel arches the following parameters were used: cross section  $A = 0.005$  m<sup>2</sup>, Young's modulus  $E = 210000$  MPa, Poisson's ratio  $\nu = 0.3125$ , static friction coefficient  $\mu = 0.5$  and clamping force  $C = 0.7$  MN. Two yielding joints were used in each steel arch, one at the left and one at the right side. The steel arches were spaced by 3 m from each other.

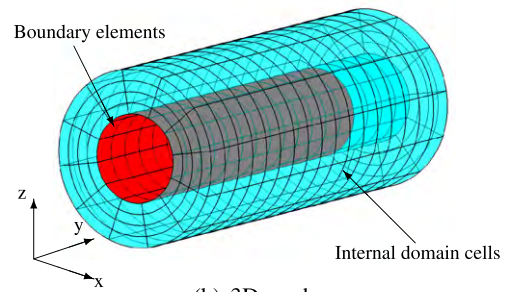
Prior to the 3D analysis, a plane strain analysis without support was carried out in order to determine the extent of the plastic zone.

Table 1  
Material properties and HMCM parameters.

Young's modulus $E$	28000 MPa
Poisson's ratio $\nu$	0.32
Cohesion $C$	12.71 MPa
Friction angle $\phi$	26.36°
Tension cutoff $p_t$	27.6 MPa
Shape parameter $Y$	0.61
Shape parameter $Z$	0.23



(a) 2D mesh



(b) 3D mesh

Fig. 20. Boundary element discretisation with internal domain cells.

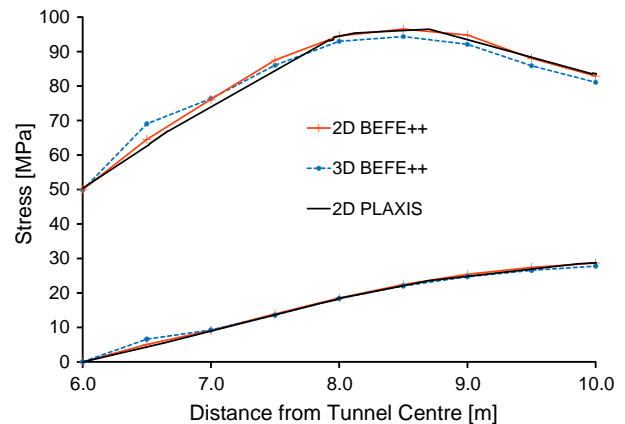


Fig. 21. Comparison of results for radial and tangential stress for a horizontal line normal to the tunnel axis.

The result is shown in Fig. 23. Fig. 24 shows the corresponding vertical displacements. However, in the following 3D analysis the extension of the plastic zone is verified for each configuration. It is pointed out that the plastic zone never exceeds the estimated plastic zone from the 2D analysis in the following 3D analyses.

Fig. 25 shows a comparison between the displacements along the tunnel crown obtained with the 3D analysis for the different configurations and support conditions. The influence of the various ground support configurations on the tunnel crown displacements

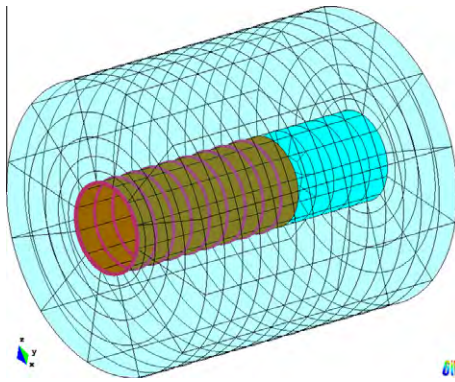


Fig. 22. Mesh discretisation with internal domain cells, shotcrete and ribs.

Table 2  
Material properties and HMC parameters.

Young's modulus $E$	258.28 MPa
Poisson's ratio $\nu$	0.25
Cohesion $C$	0.7 MPa
Friction angle $\phi$	25°
Tension cutoff $p_t$	0.10 MPa
Shape parameter $Y$	0.61
Shape parameter $Z$	0.23

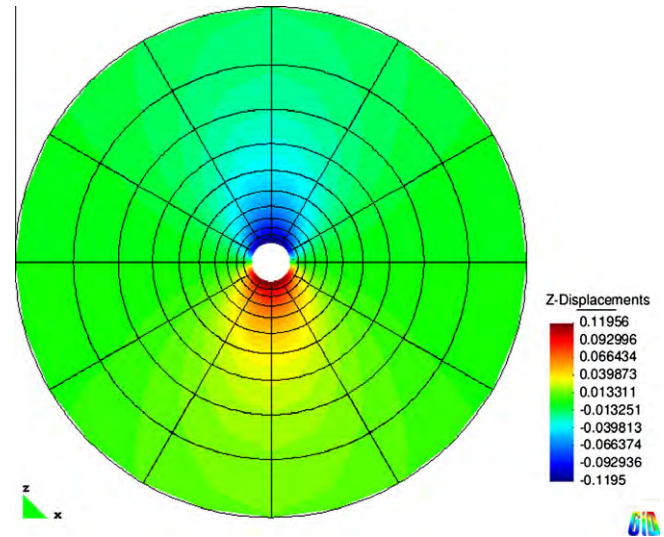


Fig. 24. Vertical displacements [m] obtained with a 2D analysis.

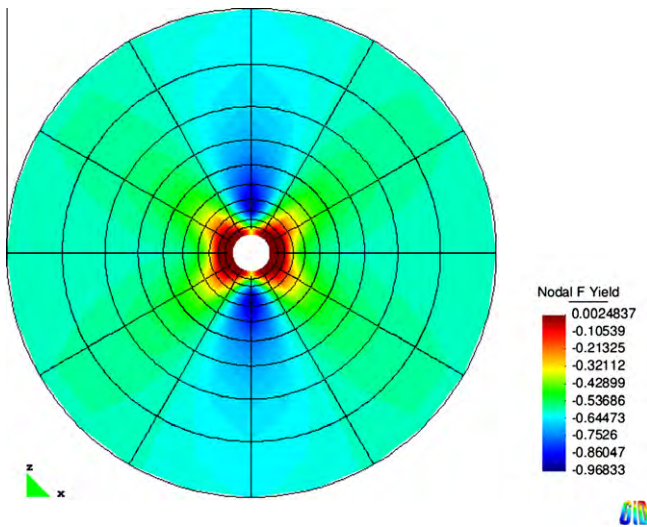


Fig. 23. Value of yield function [-] obtained with a 2D analysis.

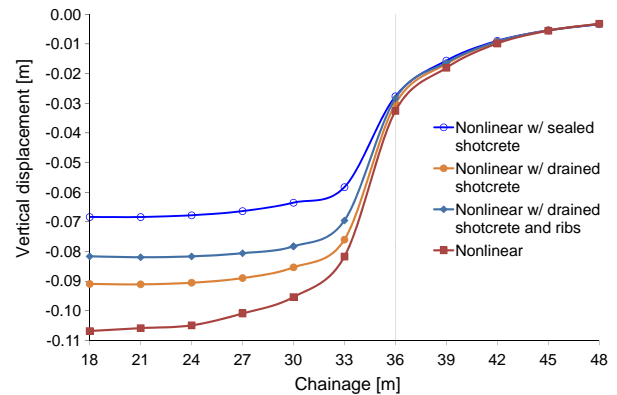


Fig. 25. Comparison between the displacement along the tunnel crown for the different support configurations.

can easily be seen. In fact it can be seen that – depending on the support condition – the displacements can be reduced up to 60% for this specific problem. In addition, it can be noted that the maximum displacement obtained from the 2D analysis (Fig. 24) and the maximum displacement obtained from the 3D analysis carried out without support (see the results of Nonlinear in Fig. 25) are very similar.

7.3. Practical example – Koralm tunnel

The Koralm tunnel is the core piece of the future high speed railway connection between Graz and Klagenfurt in Austria and also an important part of the international traffic route “ADRIATIC-BALTIC-AXIS” from Venice in Italy to Gdansk in Poland. It will underpass the Koralpe mountain located between the Austrian provinces of Carinthia (Kärnten) and Styria (Steiermark).

As shown in Fig. 26 the Koralm tunnel is a double single-track tube tunnel with a length of 32.8 km. Each tube has a cross-section of 52 m<sup>2</sup>. Approximately one quarter of the tunnel is driven into claystone, siltstone and sandstone with a maximum overburden of 200 m. The remaining three quarters are driven in crystalline bedrock with a maximum overburden of 1250 m as shown in Fig. 27. The construction work of the Koralm tunnel was started in 2008 and the scheduled date for the start of the tunnel operation is 2016.

The simulation results shown in this work are for a section of one single-track tube. The overburden in the section analysed is about 140 m and the coefficient of horizontal earth pressure has been assumed to be  $K_0 = 0.5$ . The material properties of the ground in this section are shown in Table 3.

The simulation is carried out for a full face tunnel excavation with 3 m excavation length per construction stage. The HMC is used for the nonlinear material behaviour. The tunnel is supported by a 35 cm thick shotcrete-shell. The changing material properties of the shotcrete during the hydration time for sealed shotcrete condition with  $w/c = 0.4$  and  $a/c = 3.5$ , using the look-up tables presented in Section 4.1.2. The boundary element mesh with the internal domain cells for plasticity and the shotcrete-shell elements is shown in Fig. 28.

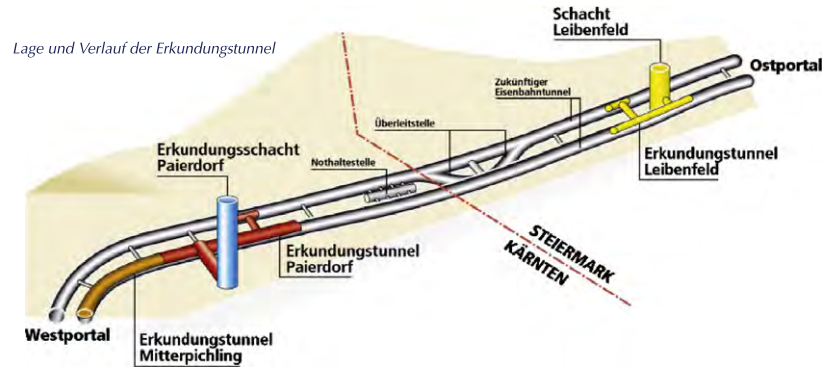


Fig. 26. Schematic drawing of the Koralm tunnel [6].

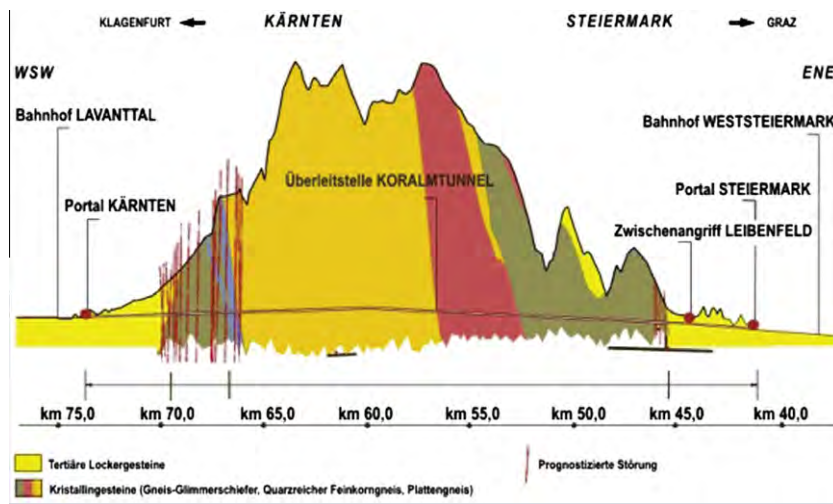


Fig. 27. Longitudinal profile of the Koralm tunnel [6].

**Table 3**  
Material properties and HMCM parameters.

Young's modulus $E$	258.28 MPa
Poisson's ratio $\nu$	0.25
Cohesion $C$	0.12 MPa
Friction angle $\phi$	30.95°
Tension cutoff $p_t$	0.05 MPa
Shape parameter $Y$	0.61
Shape parameter $Z$	0.23

The deformed shape and the contours of vertical displacements along the tunnel with the shotcrete support are shown in Fig. 29. Fig. 30 shows the contours of the tangential forces in the shotcrete shell as a consequence of the deformation in the tunnel, whereas Figs. 31 and 32 show the related contours of the moments in  $x$ - and  $y$ -direction in the shotcrete shell.

To show the accuracy and the applicability of the method applied in this work, the vertical displacement along the tunnel crown obtained in the analysis is first compared with the displacement obtained with a FDM analysis carried out with Flac3D (Fig. 33) and second with the displacement measured in the field (Fig. 34). Note that in Fig. 33 the total displacements along the tunnel crown are compared, while in Fig. 34 the relative displacements with respect to the reference measuring point near to the tunnel face are compared. It can be seen that both the Flac3D

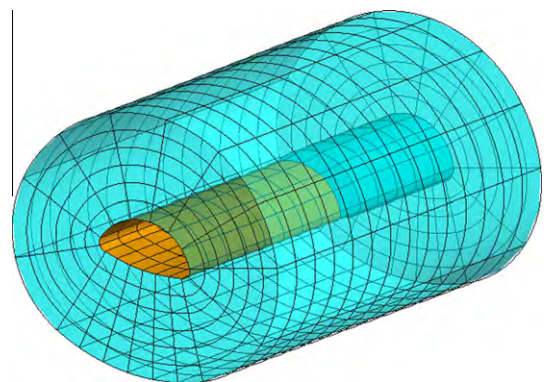


Fig. 28. Boundary element mesh with internal domain cells and shotcrete-shell elements.

analysis and the field measured data agree very well with the results obtained in this work.

**8. Conclusions**

This paper presents a new approach to simulate real 3D NATM tunnelling problems. The BEM is used as principal numerical method and it handles the whole rock mass including the regions which

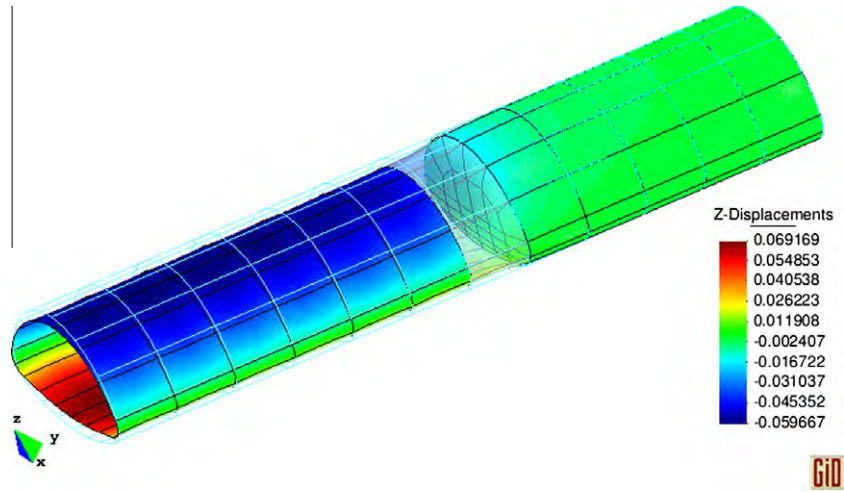


Fig. 29. Deformed shape and contour of vertical displacements [m].

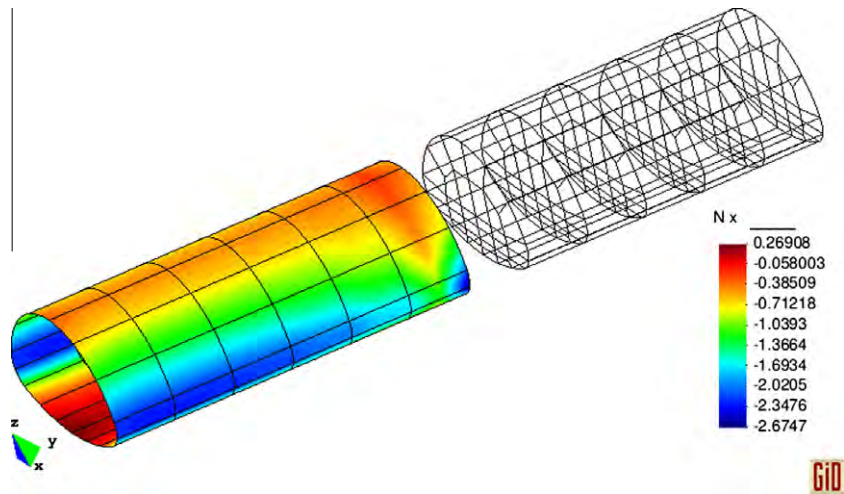


Fig. 30. Contour of shotcrete forces [MN] in tangential direction.

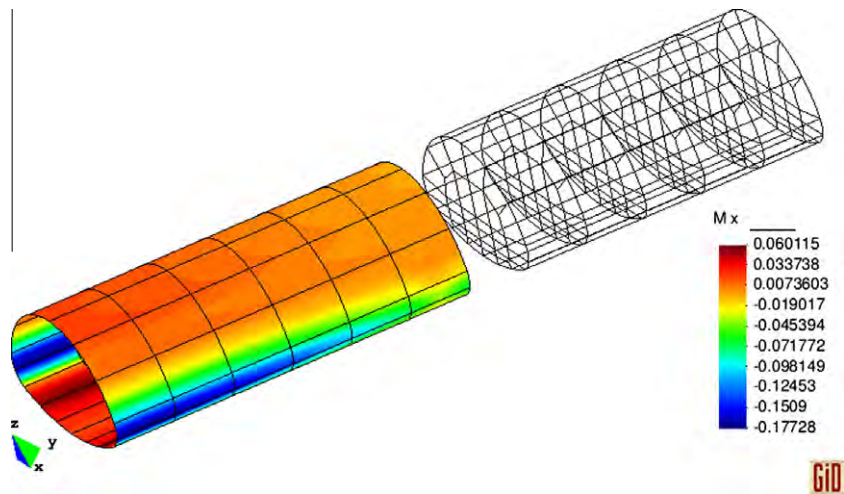


Fig. 31. Contour of shotcrete moments  $M_x$  [MNm].

undergo plastic deformation. The FEM is used for the tunnel lining only and shell finite elements and beam finite elements are directly coupled to the 3D boundary elements. Therefore, a coupling strat-

egy using a pseudo interface stiffness matrix for the boundary element region has been developed. Furthermore, the multiregion approach has been used in order to simulate the sequential

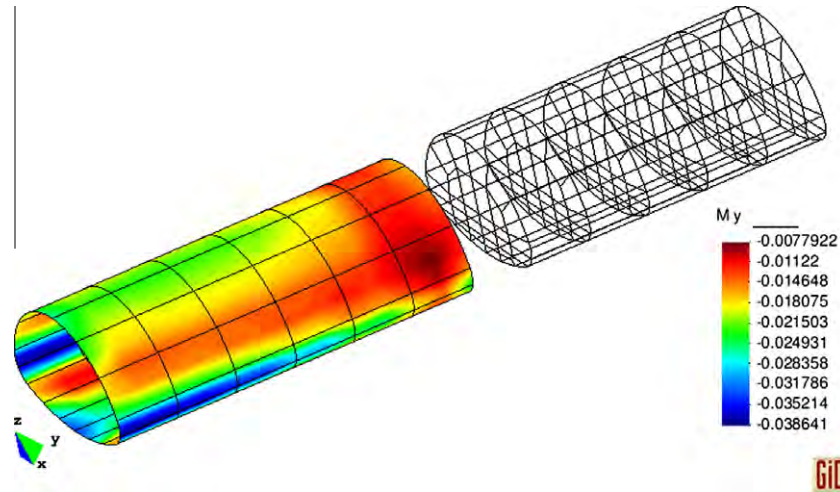


Fig. 32. Contour of shotcrete moments  $M_y$  [MNm].

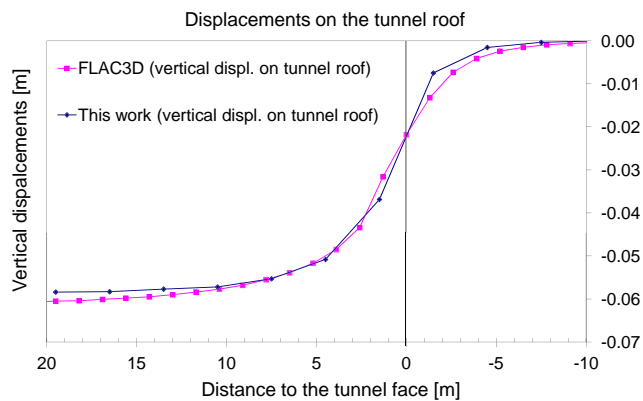


Fig. 33. Comparison between presented analysis and Flac3D.

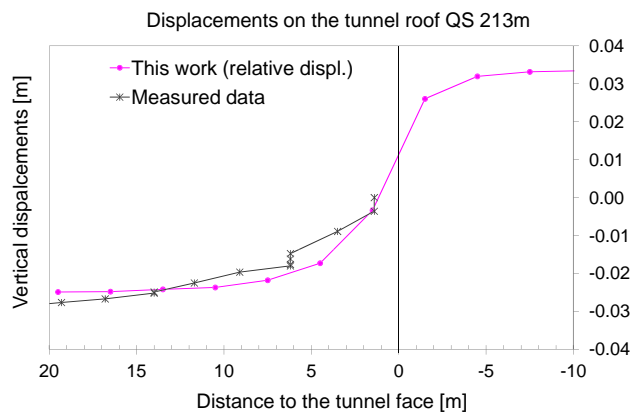


Fig. 34. Comparison between computed and measured results.

excavation process with the BEM. Special emphasis has been placed on the realistic simulation of the tunnel lining. Both the evolution of the shotcrete strength due to hydration and the yielding connections in the steel arches have been taken into account. In order to realistically consider the nonlinear behaviour of the rock mass a hierarchical constitutive model able to span the full range of rock materials has been introduced.

Finally, test examples showing the accuracy and the efficiency of the new method have been presented. The new approach has

also been applied to a practical example where the results agree with the results from a Flac3D analysis and the field measured data. This shows that the approach presented in this work can be successfully applied to solve real 3D tunnelling problems. From the practical point of view the advantage of easy mesh generation and the prevention of introducing artificial boundary conditions are significant advantages over domain based methods.

#### Acknowledgements

The work depicted here is a result of a research initiative of the Institute for Structural Analysis of Graz University of Technology to develop a practical and efficient finite element and boundary element program (BEFE++) that can be applied to tunnelling problems. The support of the European Commission of the integrated project TUNCONSTRUCT is gratefully acknowledged. The authors are grateful to Bernhard Pichler for supplying the look-up tables for shotcrete. The Subroutines for the hierarchical material model were supplied by the group of Antonio Gens at UPC. The authors are grateful for the permission to use them. Moreover, the authors would like to thank the three anonymous reviewers for their valuable comments and constructive suggestions for improving the original manuscript.

#### References

- [1] Ahmad S, Irons BM, Zienkiewicz OC. Analysis of thick and thin shell structures by curved finite elements. *Int J Numer Meth Eng* 1970;2:419–51.
- [2] Anagnostou G, Cantiati L. Design and analysis of yielding support in squeezing ground. In: 11th ISRM congress, the second half-century of rock mechanics, July 9–13. Lisbon, Portugal; 2007.
- [3] Banerjee PK. The boundary element methods in engineering. London: McGraw-Hill Book Company; 1994.
- [4] Bathe K-J. Finite element procedures. New Jersey: Prentice-Hall; 1996.
- [5] Beer G. Programming the boundary element method. An introduction for engineers. Chichester: John Wiley & Sons, Ltd; 2001.
- [6] Beer G, editor. Technology innovation in underground construction. Taylor and Francis Group; 2009.
- [7] Beer G, Smith I, Duenser C. The boundary element method with programming. Wien: Springer-Verlag; 2008.
- [8] Beer G, Watson JO. Introduction to finite and boundary element methods for engineers. Chichester: John Wiley & Sons, Ltd; 1992.
- [9] Butterfield R, Tomlin GR. Integral techniques for solving zoned anisotropic continuum problems. In: International conference variational methods in engineering. Southampton University; 1972. p. 9/31–53.
- [10] Cisilino AP, Aliabadi MH. A boundary element method for three-dimensional elastoplastic problems. *Eng Comput* 1998;15(8):1011–30.
- [11] Davies TG, Gao X-W. Three-dimensional elasto-plastic analysis via the boundary element method. *Comput Geotech* 2006;33(3):145–54.

- [12] Duenser C. Simulation of sequential tunnel excavation with the boundary element method. Monographic Series TU Graz: Structural Analysis. Verlag der Technischen Universität Graz; 2007.
- [13] Gao X-W, Davies TG. Boundary element programming in mechanics. Cambridge: Cambridge University Press; 2002.
- [14] Gens A, Carol I, Gonzales N, Caballero A, Garolera D. Library of model subroutines soil and rock models. In: TunConstruct Deliverable 1.1.1.4; 2007.
- [15] Gioda G, Swoboda G. Developments and applications of the numerical analysis of tunnel in continuous media. *Int J Numer Anal Meth Geomech* 1999;23:1393–405.
- [16] Podjadtke R, Witthaus H, Breedlove J. Development in steel roadway support – a track record. In: 27th International conference on ground control in mining; 2008. p. 8.
- [17] Pöttler R, Swoboda GA. Coupled beam-boundary-element model (BE-BEM) for analysis of underground openings. *Comput Geotech* 1986;2(4):239–56.
- [18] Prazeres P. Simulation of NATM tunnel construction with the BEM. Monographic Series TU Graz: Structural Analysis. Verlag der Technischen Universität Graz; 2010.
- [19] Scheiner S, Pichler B, Hellmich C. From micron-sized needle-shaped hydrates to meter-sized shotcrete tunnel shells: micromechanical upscaling of stiffness and strength of hydrating shotcrete. *Acta Geotechnica* 2008;3:273–94.
- [20] Shou K. A three-dimensional hybrid boundary element method for non-linear analysis of a weak plane near an underground excavation. *Tunnel Undergr Space Technol* 2000;15(2):215–26.
- [21] Souza Neto EAd, Perić D, Owen DRJ. Computational methods for plasticity: theory and applications. Chichester: John Wiley & Sons, Ltd; 2008.
- [22] Swoboda G, Mertz W, Beer G. Rheological analysis of tunnel excavations by means of coupled finite element (FEM)- boundary element (BEM) analysis. *Int J Numer Anal Meth Geomech* 1987;11:115–29.
- [23] Telles JCF. The boundary element method applied to inelastic problems. Berlin: Springer-Verlag; 1983.
- [24] Telles JCF, Brebbia CA. On the application of the boundary element method to plasticity. *Appl Math Model* 1979;3(6):466–70.
- [25] Thoeni K. The boundary element method for non-linear problems: a novel approach for an error-controlled adaptive analysis. Monographic Series TU Graz: Structural Analysis. Verlag der Technischen Universität Graz; 2009.
- [26] Varadarajan A, Sharma KG, Singh RB. Elasto-plastic analysis of an underground opening by FEM and coupled FEBEM. *Int J Numer Anal Meth Geomech* 1987;11:475–87.
- [27] Venturini WS, Brebbia CA. Boundary element formulation for nonlinear applications in geomechanics. *Appl Math Model* 1984;8(4):251–60.
- [28] Wang CB, Chatterjee J, Banerjee PK. An efficient implementation of BEM for two- and three-dimensional multi-region elastoplastic analysis. *Comput Meth Appl Mech Eng* 2007;196(4-6):829–42.
- [29] Xiao B, Carter JP, Alehossein H. Elastoplastic analysis of jointed rocks using a coupled finite element and boundary element method. *Int J Numer Anal Meth Geomech* 1994;18(7):445–66.
- [30] Zienkiewicz OC, Taylor RL. The finite element method. Boston: Butterworth Heinemann; 2000.